Size Dependent Reaction Kinetics on Supported Model Catalysts: A Molecular Beam/IRAS Study of the CO Oxidation on Alumina-Supported Pd Particles

I. Meusel, J. Hoffmann, J. Hartmann, J. Libuda,* and H.-J. Freund

Fritz-Haber-Institut der Max-Planck-Gesellschaft, Faradayweg 4-6, D-14195 Berlin, Germany

Received: October 2, 2000; In Final Form: February 6, 2001

We have employed molecular beam techniques combined with in situ IR reflection absorption spectroscopy to study the CO oxidation kinetics on oxide-supported model catalysts. As model systems we utilize Pd particles of different size and morphology grown under ultrahigh vacuum conditions on a well-ordered alumina film on NiAl(110). Previously, these systems have been characterized in detail with respect to their geometric and electronic structure. Using a combination of two beam sources crossed on the sample surface, the transient behavior and the steady-state reaction rate are systematically probed over a wide range of CO and oxygen fluxes and at different sample temperatures. Comparing different particle sizes and structures, characteristic differences are observed with respect to both the steady-state reaction rate and the transient behavior upon switching off the CO beam source. The origin of these effects is discussed with respect to the different CO and oxygen adsorption properties of small Pd particles. To directly monitor changes in the CO adsorption during the reaction, we have performed in situ IR absorption spectroscopy under steady-state conditions. Whereas strong rearrangements of the CO adsorbate layer are found for large and well-ordered particles as a function of the applied CO and oxygen fluxes, no similar effects are observed on small Pd aggregates.

1. Introduction

Typically, heterogeneous catalysts are complex systems with properties sensitively depending on their composition and preparation procedure.[1] Specifically with respect to supported metal catalysts, it is widely accepted that the activity and selectivity of those systems may be strongly influenced by the support and the particle size.[2] Many concepts have been proposed which may possibly explain the molecular origin of the modified reaction kinetic kinetics. Among these are, for example, size effects;[3,4] geometrical effects, due to the presence of specific adsorption sites or the combination of adsorption sites (see, for example, refs 5 and 6); the influence of boundary sites at the metal oxide interface;[7] metal support interactions;[8−10] or support effects (see, for example, refs 6, 11, and 12 and refs. therein). One aspect that makes the reaction kinetics on supported catalyst inherently different from single crystal surfaces is the simultaneous presence of a variety of nonequivalent sites in close proximity, such as different crystallite facets, edge, defect, or particle boundary sites. In recent Monte Carlo simulations, Zhdanov and Kasemo have demonstrated that the coupling between such nonequivalent adsorption sites by diffusion might substantially alter the observed reaction rates.[13−15]

Unfortunately, specific experimental evidence for the concepts mentioned before are extremely scarce. This is due to the fact that real catalysts are usually hardly accessible to surface science experiments and their vast complexity often precludes an assignment to specific microscopic properties. On the other hand, the effects will not be present on experimentally easily accessible single-crystal surfaces. To overcome this so-called "materials gap" between surface science and catalysis (see, for example, refs 16 and 17), a variety of supported model catalysts have been developed. These models allow us to introduce certain aspects of a real catalysts in a more controlled fashion, while the experimental accessibility is still maintained (see refs 6, 17−21).

The development of such model systems requires several steps, as can be illustrated for the $Pd/Al_2O_3/NiAl(110)$ catalyst employed in this work: First, the structure and defect structure as well as the adsorption properties of the Al_2O_3 film were investigated.[22−24] Subsequently, the growth, geometric structure, and electronic structure of Pd particles supported on this film and their adsorption properties have been addressed in a series of studies.[17−19,21,25−27] On the basis of this work we finally attempt to establish a correlation between the structure and the microscopic kinetics.

Providing a maximum of control over the reactants, molecular beam techniques represent the method of choice in this type of microkinetic studies.[28−31] Ertl and Engel[32,33] earlier applied beam methods to study the kinetics of the CO adsorption and oxidation on Pd(111), and a variety of similar studies on other single-crystal surfaces have been published since (see refs 34−36). Despite the successful experiments on single crystals, similar beam studies on supported catalysts are, however, scarce and contradictory (see ref 6 and refs therein). It remains unclear to what extent size effects may influence the kinetics and energetics of the reaction.[37−41]

For example, Becker and Henry have investigated the CO oxidation on Pd/MgO(100) model catalysts by molecular beam methods and related the transient effects in the reaction rate to defect adsorption.[39,40] In a recent work, however, we have shown that similar transients may be observed on larger, well-ordered particles and can be understood without the assumption of strong CO adsorption at defects.[42] In this study, we will extend the previous work to a comparison of different types of Pd particles. It is shown that there indeed exist pronounced differences in the transient and steady-state kinetics as a function of particle size.

* Corresponding author. FAX: +49-30-8413-4309. E-mail: libuda@fhi-berlin.mpg.de.

10.1021/jp003601l CCC: $20.00
Published on Web 04/11/2001

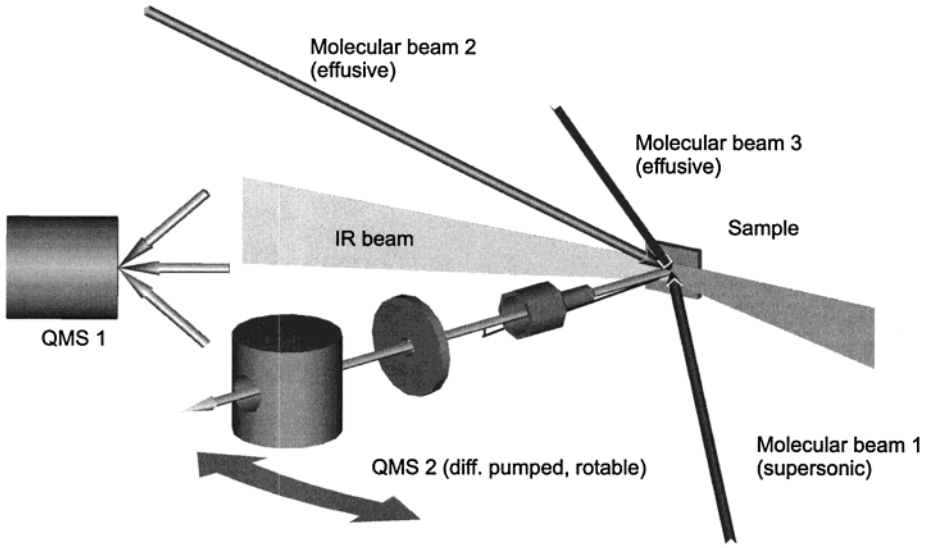

Figure 1. Schematic representation of the molecular beam/IR spectroscopy experiment.

TABLE 1: Preparation Conditions and Structural Parameters for the Pd Particles on Al_2O_3/NiAl(110)

	type I Pd particles	type II Pd particles
deposition parameters		
Pd coverage (atoms·cm^{-2})	2.7×10^{15}	0.7×10^{15}
deposition temperature (K)	300	90
deposition rate (atoms·cm^{-2}·s^{-1})	9×10^{12}	$(5-9) \times 10^{12}$
structural parameters		
island density (cm^{-2})	$1.0\ (\pm 0.2) \times 10^{12}$ [25,41]	$6.5\ (\pm 2) \times 10^{12}$ [60]
no. of Pd atoms/island	~ 2700 [25,41]	~ 100 [60]
estimated fraction of support covered by Pd	$\sim 0.20\ (\pm 0.02)$ [44]	$\sim 0.15\ (\pm 0.05)$
estimated fraction of surface Pd atoms	$0.20\ (\pm 0.03)$ [44]	$0.6\ (\pm 0.1)$
average island size (nm)	$\sim 5.5 \pm 0.7$	$\sim 1.8 \pm 0.4$
epitaxial orientation	(111) [25]	–
island structure	crystalline, predominantly (111) facets, small fraction of (100) facets [25,27]	irregular, no indications for ordered facets, hemispherical [25]

2. Experimental Section

All experiments were performed in a ultrahigh vacuum (UHV) molecular beam/surface spectroscopy apparatus, which has been described recently in the literature.[43] A schematic representation of the experiment is displayed in Figure 1.

The system was specifically designed for kinetic studies on complex model systems. It offers the experimental possibility of up to three beams being crossed on the sample surface. The CO and O_2 beams that were used in the work presented here are generated by two effusive sources based on multichannel arrays. This design allows an easy variation of the beam intensities over several orders of magnitude, without any change in the beam properties. Beam modulation is provided by a computer-controlled shutter located inside the second pumping stage of the beam sources or electropneumatically operated inlet valves, respectively. To avoid artifacts due to only partial overlap, the beam diameter was chosen such that it exceeds the sample surface. The mean beam intensity variation over the sample surface was determined to be 6%, and the average variation in the CO/O_2 beam intensity ratio over the sample surface was estimated to be less than 2% (from beam profile measurements). Both sources were operated at room temperature. High purity oxygen (AGA, >99.999%) and CO (AGA, >99.996%) were used, the latter of which was further purified using an N_2 cold trap. Beam intensities and profiles were measured with a beam monitor, as described elsewhere.[43] The third source generates a beam from a supersonic expansion and has not been used in the present study.

Angular-integrated gas-phase measurements were performed with a quadrupole mass spectrometer (ABB Extrel), which is not in the line-of-sight of the sample. Additionally, the system allows time- and angular-resolved measurements via a differentially pumped rotatable quadrupole mass spectrometer. The gas-phase detection can be combined with time-resolved in situ FT-IR reflection absorption spectroscopy (TR−IRAS) employing a vacuum FT-IR spectrometer (Bruker). A MIR polarizer was used to select only the p-component of the IR light and thus further improve the S/N ratio. For a detailed description of the experimental details, we again refer to the literature.[43] All spectra were recorded at a spectral resolution of 8 cm^{-1}. The total acquisition time for the in situ IR spectra was typically 50 s.

Briefly, the sample was prepared by sputtering and annealing of a NiAl(110) single crystal, followed by an oxidation and annealing procedure, the details of which are given elsewhere.[22,23] The cleanliness and quality of the oxide film was checked via LEED (low-energy electron diffraction) and AES (Auger electron spectroscopy). Before the actual experiment, the active metal component (Pd, >99.9%) was deposited under well-controlled conditions by evaporation from a rod (1 mm diameter) using a commercial evaporator (Focus, EFM 3) based on electron bombardment. During deposition, the crystal was biased with a retarding voltage in order to prevent ions from being accelerated toward the sample (point defect creation). The evaporator flux was calibrated by a quartz microbalance prior to use. Details concerning typical deposition rates and conditions are given in Table 1. After preparation the Pd particles were stabilized by oxygen and CO exposure as discussed previously.[41]

3. Results and Discussion

3.1. Characterization of the Structural and Adsorption Properties of the Supported-Pd Model Catalyst. Before considering the CO oxidation kinetics on the supported model catalyst, we will briefly summarize those aspects of the structural and adsorption properties of the Pd particles that are of relevance for the following discussion. The growth and structure of Pd deposits on Al_2O_3/NiAl(110) as well as the adsorption of CO have previously been studied over a wide range of deposition parameters.[18,19,25−27] In this work, we will compare two specific types of Pd aggregates, which, in the following, will be denoted as Pd particles of type I and type II, respectively. For use in the discussion, the most relevant structural information is summarized in Table 1. All data was derived from STM or high-resolution LEED measurements. More details on the corresponding experiments can be found in the literature.[25,27,41,44]

Type I Particles. At a growth temperature of 300 K, large and well-shaped particles are formed that grow in (111)-orientation, preferentially exposing (111)- and only a small fraction of (100)-facets. At the metal coverage used in this work (2.7×10^{15} atoms cm^{-2}), their density typically amounts to 1×10^{12} islands cm^{-2}. It can be estimated that the average Pd particle will contain about 2700 atoms, corresponding to a particle size of 5.5 ± 0.7 nm. In Figure 2 typical STM images[41] for particles of this type are displayed (please note that in the STM image the islands appear larger than the above value due to an instrumental convolution with the tip shape). In a series of previous experiments it has been shown that the Pd particles of type I in many ways resemble the typical properties of a Pd(111) surface. For example, we have probed the CO adsorption/desorption kinetics employing modulated molecular beam techniques and have determined activation energies for desorption which are in good agreement with Pd(111) single-crystal data.[33] Also, the thermal desorption spectra for CO[25,45] are similar to those of Pd(111)[46] and so are the activation barriers for the Langmuir−Hinshelwood reaction step of the CO oxidation.[41]

Type II Particles. As a second model system we will use small Pd particles grown at a substrate temperature of 90 K. In Figure 2b a STM image is shown for such aggregates that were prepared at 90 K and that, similar to the reactivity experiments in this work, were heated to 500 K, subsequently. At low deposition temperature, the reduced diffusion length results in an increased nucleation density. Thus an increased island density (6.5×10^{12} islands cm^{-2}) and consequently smaller islands (100 atoms island^{-1} or about 1.8 ± 0.4 nm particle size at a Pd coverage of $0.7 \cdot 10^{15}$ atoms cm^{-2}) are formed. In contrast to the particles grown at 300 K, neither high-resolution LEED nor STM have shown any indications for the formation of well-ordered facets. In previous studies small particles of type II have been shown to exhibit a strongly modified adsorption behavior toward CO.[45,25] In TPD (temperature programmed desorption) experiments, an increased population of weakly bound CO is detected, besides the regular CO desorption features in the temperature region between 450 and 500 K typical for Pd(111) and -(100).[46,47] PES (photoelectron spectroscopy) and XAS (X-ray absorption spectroscopy) point to a stronger coverage dependence of the CO−Pd bond strength.[25,48] Via PES measurements and IRAS, the modified adsorption behavior at lower temperature was demonstrated to be correlated to an increased population of lower coordinated (on-top) sites.[25,26]

Before the kinetic experiments both types of particles were stabilized by extended oxygen exposure (experimental conditions, typically $\sim 3 \times 10^{-7}$ Torr for 1000 s at a sample temperature of 400 K), followed by CO oxidation cycles of the type shown in this work. Previously, this stabilization procedure has been shown to be necessary to obtain a stable oxidation kinetics.[41] It was suggested that the behavior is connected to a bulk diffusion process of oxygen under reaction conditions. As observed by STM[41] for type I particles, neither the island density nor the shape are significantly affected by this procedure.

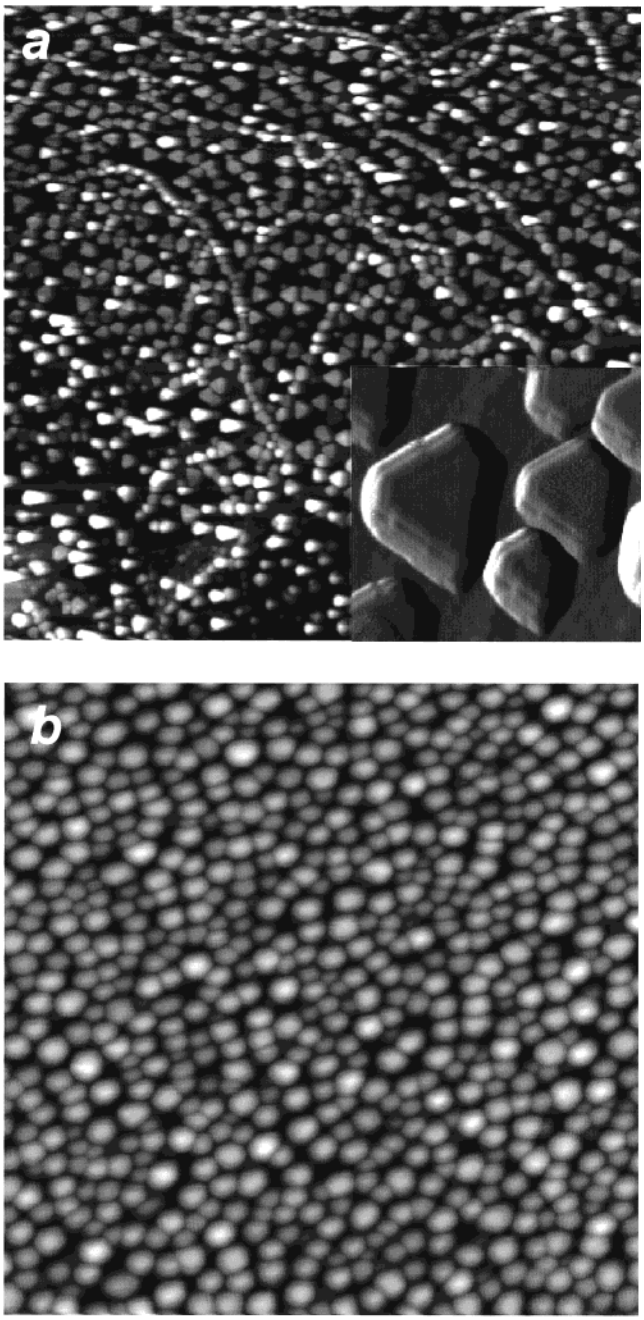

Figure 2. (a) STM image (CCT, constant current topography, 3000 Å × 3000 Å) of Pd particles (2.7×10^{15} Pd atoms·cm^{-2}) grown at 300 K on Al_2O_3/NiAl(110); the inset shows a differentiated close-up STM image of the particles (CCT, 200 Å × 200 Å);[41] (b) STM image (CCT, 1000 Å × 1000 Å) of Pd particles (1.1×10^{15} Pd atoms·cm^{-2}) grown at 90 K on Al_2O_3/NiAl(110) after heating to 500 K.[64]

A final remark before discussing the reactivity measurements is related to the catalyst stability under the reaction conditions applied in this study. Processes that may influence the catalytic activity include (a) structural rearrangements or changes in the particle dispersion (see ref 49) and (b) a buildup of surface carbon as a result of CO dissociation.[50] To probe whether there

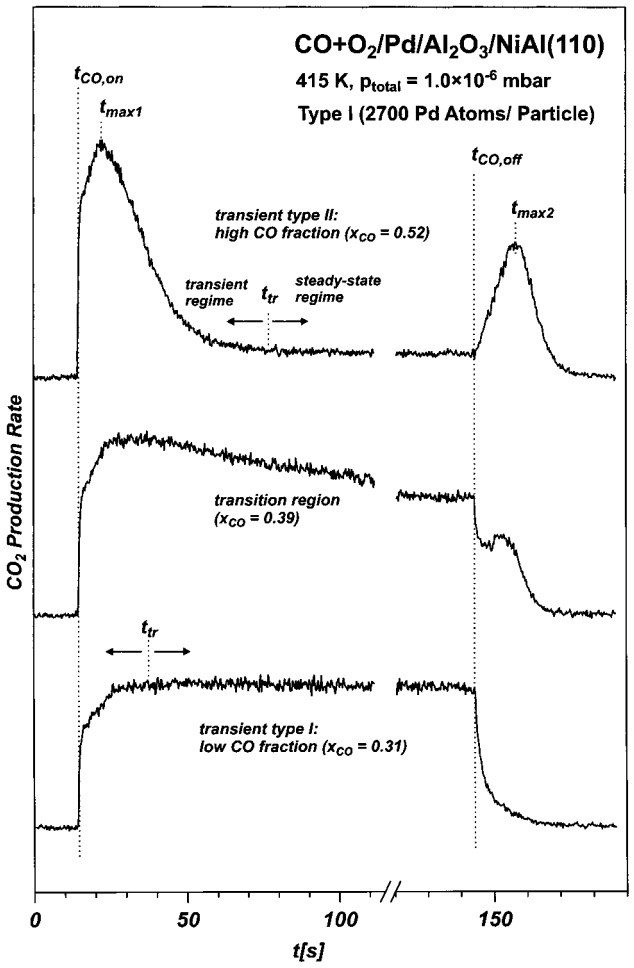

Figure 3. Transient behavior of the CO_2 production rate (continuous O_2 beam and a modulated CO beam) under CO-rich conditions (upper trace, transient type II), under O_2-rich conditions (lower trace, transient type I) and in the transition region between the two regimes (middle trace) (T_{sample} = 415 K, $p_{total} = 1.0 \times 10^{-6}$ mbar).

is a significant deactivation on the time-scale of the experiment, we have performed transient reactivity measurements of the type shown in the following section at regular intervals and under identical conditions. For Pd particles of both types, there was no detectable indication for a significant deactivation of the model catalysts within the reaction times and gas exposures used in this work. Minor variations in the transient behavior can be related to the bulk diffusion process, which may be not be fully completed during the stabilization procedure (see also discussion in ref 42).

3.2. Systematic Studies of the Transient Behavior and Steady-State CO_2 Production. In this work we will present a series of transient reactivity experiments over a large range of flux and temperature conditions. Before we will come to a discussion of the particle size dependence of the kinetics, we will give a short description of how most of the experiments in this study were performed and how the different types of transients can be qualitatively understood. A more detailed discussion can be found elsewhere.[42,51]

We consider the experiments displayed in Figure 3, which were performed in the following manner: After preparation and stabilization of the model system, the surface is continuously exposed to an O_2 beam with a beam flux F_{O_2}, generated by one of the effusive beam sources. The integral CO_2 production rate is recorded simultaneously. At a given time (see Figure 3) a CO beam with a beam flux F_{CO}, generated by the second effusive source, is switched on. After the steady-state reaction rate is reached, the CO beam is switched off (see Figure 3). Thus for every set of experimental conditions two types of transient CO_2 curves and the steady-state reaction rate are obtained. Additionally, a IRA spectrum is recorded for every set of steady-state conditions (see section 3.3). We characterize the reactant flux defining the two parameters: (1) x_{CO}, the CO fraction with respect to the total flux

$$x_{CO} = \frac{F_{CO}}{F_{CO} + F_{O_2}} \tag{1}$$

and (2) p_{total}, the total effective pressure of CO and O_2 at the sample position

$$p_{total} = p_{CO} + p_{O_2} \qquad \text{with} \quad p_i = F_i(2\pi m_i kT)^{0.5} \tag{2}$$

where F_i is the partial flux of component i at the sample position, m_i represents its molecular mass, and T_i is the temperature describing the velocity distribution (please note that T_i = 300 K, as there is no cooling of any degree of freedom in the effusive sources). In a typical series of experiments such as displayed in Figure 4, the CO flux fraction was varied, whereas the total effective pressure was kept constant by adjusting the CO and O_2 partial fluxes.

As a function of the CO flux fraction, two characteristic types of transients and a transition regime are observed. The transients are related to the so-called oxygen-rich and CO-rich regime of reaction conditions, respectively. Briefly, the qualitative behavior can be understood as follows (a more detailed discussion can be found elsewhere[42,51]):

Oxygen-Rich Regime, Transient Type I. An example for the transient behavior under oxygen-rich reaction conditions is displayed in the lower trace in Figure 3 (x_{CO} = 0.31). Starting from a situation in which the system has reached its oxygen saturation coverage, we find an instantaneous—on the time-scale of the experiment—increase in the CO_2 production upon switching on the CO beam. This is due to the rapid formation of a steady-state precursor coverage.[51] From the precursor state, the CO molecule may either desorb or chemisorb and subsequently react to CO_2. During the reaction oxygen vacancies are generated, which lead to an increased chemisorption probability of the CO precursor and thus a slow increase in the reaction rate. Finally, the system reaches the steady-state, which is characterized by a high oxygen and a small CO coverage. After switching off the CO beam, the adsorbed CO is rapidly consumed and the CO_2 production rate decreases.

CO-Rich Regime, Transient Type II. A typical transient under CO-rich conditions is shown in the upper trace in Figure 3 (x_{CO} = 0.52). Again, we start from an oxygen-saturated surface. Similarly to the transients under oxygen-rich conditions, an instantaneous CO_2 production is found upon switching on the CO beam, followed by a slower increase, which again can be explained by the increasing chemisorption probability of the CO precursor due to the decreasing oxygen coverage.[51] With CO accumulating on the surface, however, the oxidation rate finally starts to decrease as a consequence of the strongly inhibiting effect of CO on the O_2 adsorption (see ref 52 and refs therein), resulting in a first maximum in the reaction rate (t_{max_1}). The steady-state under these conditions is characterized by a high CO coverage and a low reaction rate. Upon switching off the CO beam, the adsorbed CO is consumed, leaving free adsorption sites for O_2 adsorption. The accelerated O_2 adsorption

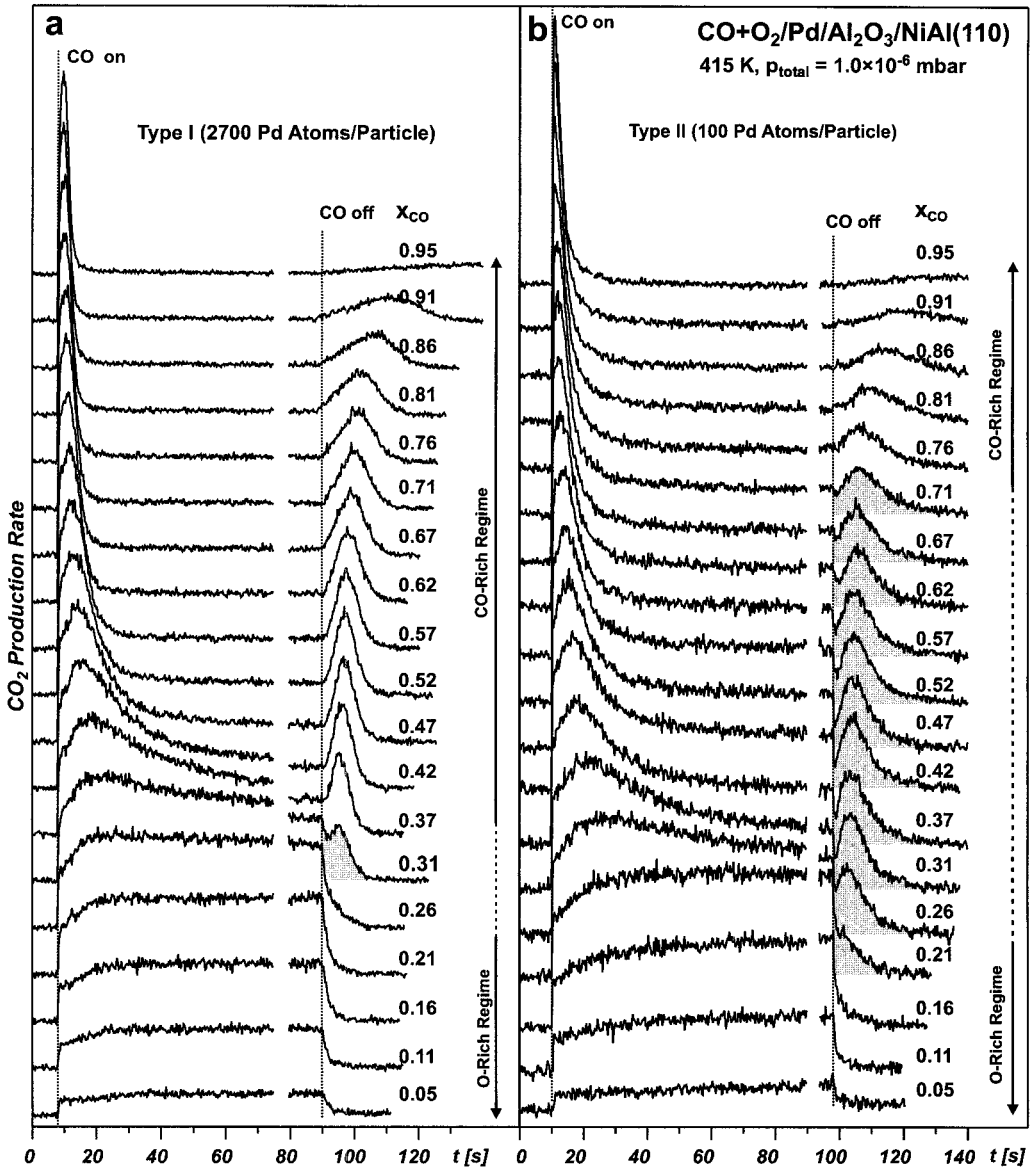

Figure 4. Transient behavior of the CO_2 production rate (for a continuous O_2 beam and a modulated CO beam) as a function of the CO fraction in the impinging gas flux x_{CO} (T_{sample} = 415 K, p_{total} = 1.0 × 10^{-6} mbar) for two different average particle sizes: (a) 2700 atoms/particle, Table 1, type I); (b) 100 atoms/particle, Table 1, type II).

leads to a second reaction rate maximum (t_{max_2}), before the rate finally becomes limited by depletion of the CO reservoir.

Transition Regime. Between the limiting cases of CO-rich and oxygen-rich reaction conditions a transition regime exists, which is characterized by the type of transient displayed in the middle trace in Figure 3 (x_{CO} = 0.39). Here, we find an initial sudden decrease in the reaction rate upon termination of the CO beam, followed a CO production peak at later time. This behavior was originally observed by Becker and Henry[39,40] and related to an initial rapid desorption from facets, followed by reaction of more strongly adsorbed CO at defect sites. However, we have recently shown for Pd particles of type I that the transition behavior is not directly related to strong adsorption at defect sites.[42] Instead, it was demonstrated that the effect can be qualitatively modeled by assuming a homogeneous surface and may arise from the CO-induced inhibition of oxygen adsorption. Additionally, the width of the transition region may be enhanced by the heterogeneity of the model catalyst, i.e., by the fact that the effective reactant flux per active Pd site, the average reaction, and desorption rates may vary drastically between the particles and thus may lead to a distribution of different steady states on separate particles (see discussion in ref 42).

In the previous work mentioned above,[42] we have focused on one type of Pd particles (type I); however, the question remains, whether there are any significant differences in the transient and steady-state kinetics as a function of particle size. To explore whether this is the case, we have compared the CO_2 production traces for the two particles types. The results for a surface temperature of 415 K are displayed in Figure 4.

Two prominent differences are observed, which are mainly related to the second CO_2 peak and the steady-state CO_2 production: (1) With respect to the steady-state reaction rate, the CO_2 peak is significantly weaker for the small particles and (2) the transition regime (i.e., the x_{CO} range where a dip in the reaction rate is observed; see marked transient regions in Figure 4) is much narrower for the large crystallites of type I ($0.26 < x_{CO} < 0.36$), whereas it is extremely broad on particles of type II ($0.16 < x_{CO} \leq 0.76$).

As shown previously, simple kinetic models based on a

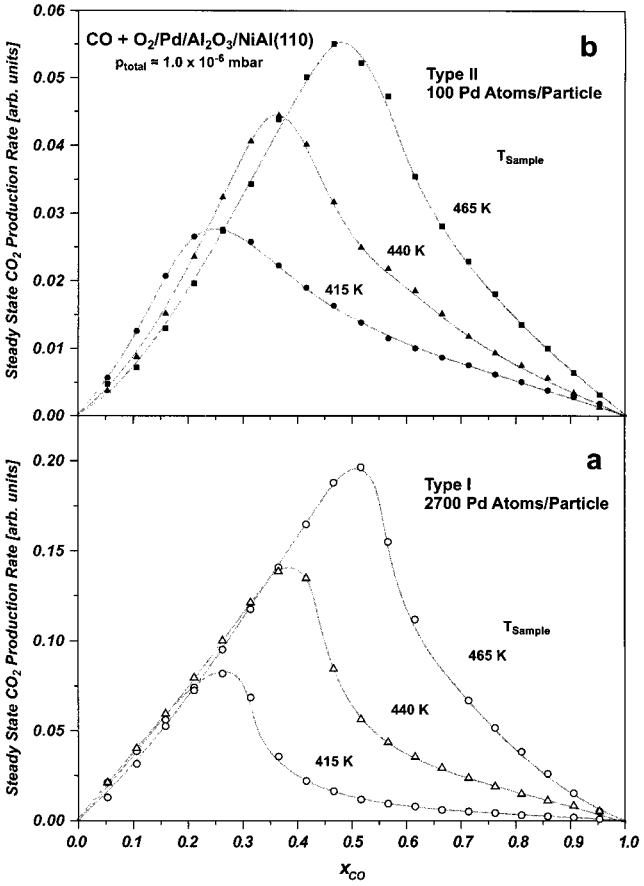

Figure 5. Steady-state CO_2 production rate as a function of the CO fraction in the impinging gas flux x_{CO}. For two different average particle sizes: (a) 2700 atoms/particle (Table 1, type I); (b) 100 atoms/particle (Table 1, type II) ($p_{total} = 1.0 \times 10^6$ mbar).

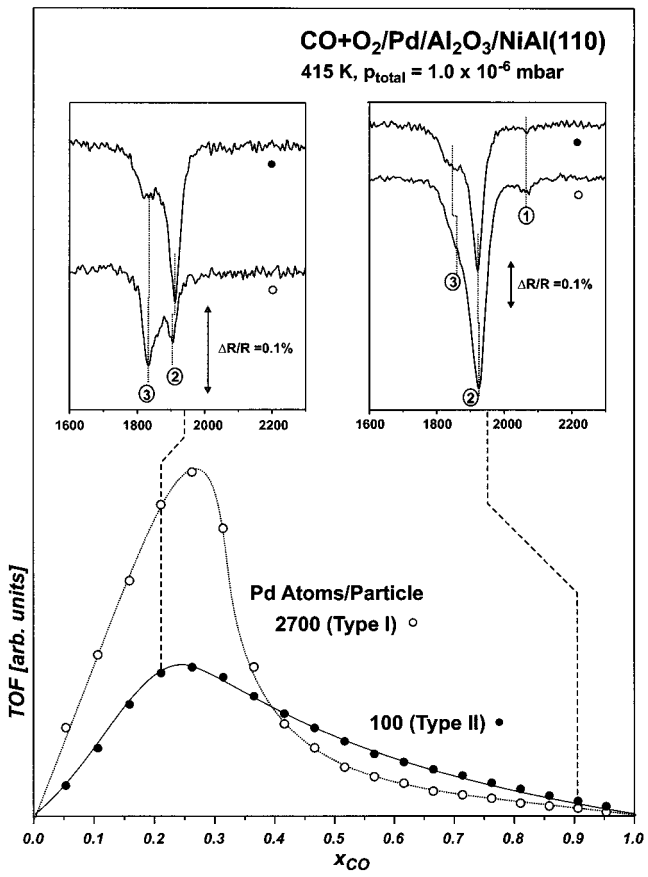

Figure 6. Turnover frequencies (steady-state reaction rates normalized to the density of Pd surface atoms) for different average particle sizes: open circles, 2700 atoms/particle (Table 1, type I); solid circles, 100 atoms/particle (Table 1, type II) ($T_{sample} = 415$ K; $p_{total} = 1.0 \times 10^6$ mbar). The inset shows the IR absorption spectra recorded under steady-state conditions for $x_{CO} = 0.21$ and $x_{CO} = 0.91$, respectively.

homogeneous[42] surface may at least semiquantitatively explain the transients for particles of type I, both with respect to the width of the transition region and the intensity of the CO_2 peak. As mentioned before, the heterogeneity with respect to particles distance, size, and structure may lead to differences in the steady states on different islands and thus enhance the effect. The extreme width of the transition region for the type II particles is, however, hardly compatible with this explanation. This is in particular the case, if we take into account that there is no indication for a more heterogeneous particle distribution from STM work (Figure 2; see also refs 19 and 25). Moreover, the weaker CO_2 production peak for type II cannot be explained by this effect. Therefore, we conclude that there is indeed an influence of the modified adsorption properties of small particles (type II) on the reaction rate.

To further explore the origin of these differences, we compare the steady-state reaction rates as a function of the CO fraction x_{CO} for the two types of Pd aggregates and different sample temperatures (Figure 5). Briefly, the two reaction regimes—oxygen-rich conditions at small x_{CO} and CO-rich conditions at large x_{CO}—can be clearly distinguished. In the oxygen-rich regime, the reaction rate increases roughly linearly with the CO flux, whereas upon transition to the CO-rich regime, the reaction rate decreases rapidly as a consequence of the inhibition of O_2 adsorption by CO. We have previously discussed this type of reactivity diagram[42] and will not repeat the details here. Instead we will focus on the *differences* as a function of particle size. The main differences which can be derived from Figure 5 are the following: (1) Under oxygen-rich conditions, the overall reaction rate is significantly reduced for the smaller particles of type II. (2) The decrease in the reaction rate under CO-rich conditions (CO poisoning) side is less pronounced for the smaller particles.

To account for the slightly different density of Pd surface area, we may normalize the reaction rates to the number of surface atoms as derived from the structure data (Table 1). Thus we derive the TOF (turnover frequency, number of product molecules per reactive site and unit time), which is displayed in Figure 6 for the two particle types and for a reaction temperature of 415 K. From the plot it becomes obvious that any comparison of reaction rates sensitively depends on the composition of the reactant gas mixture. At high oxygen flux, the activity of the small particles (type II) is reduced, whereas with increasing CO flux, the rate decrease is much weaker for the small particles and the TOF may even become larger than on the bigger particles (type I).

As mentioned in the preceding discussion, the reaction rate under oxygen-rich conditions is limited by the chemisorption rate of CO, which then is apparently lower on the small Pd particles. On supported particle systems, we have to take into account that the adsorbate flux per metal surface atom is influenced by trapping and diffusion on the support. In the special case considered in this work [homogeneous particle distribution and higher island density, but similar or smaller total density of surface atoms for the type II (small) Pd particles], we can, however, anticipate that the support trapping is similar or more efficient for the type II (small) particles as compared to the type I (large) particles. We therefore conclude that for

the small and oxygen-rich Pd particles the CO chemisorption probability is indeed reduced. A possible explanation for this phenomenon is related to the formation of subsurface oxygen. It has been shown that the rate of oxygen subsurface diffusion sensitively depends on the defect density (see refs 53−55). Thus, we may expect that on the smaller and less ordered Pd particles of type II, this oxygen interaction will be even stronger. The subsurface oxygen species can reduce the CO sticking probability/CO adsorption energy and may show a reduced reactivity toward CO. The mechanism of kinetic oscillations has been related to such a formation of subsurface oxygen.[56−58] Thus, we suggest that the lower reactivity under oxygen-rich conditions is related to the formation of such a species.

With increasing CO fraction in the impinging gas flux, the CO coverage will increase and finally—in the CO-rich regime—will result in a slow depletion of the subsurface oxygen species. Therefore, the TOF for the type II particles under CO-rich conditions is expected to approach the value for the larger type I particles, which is in line with the experimental observation under moderate CO flux (Figure 6). However, under conditions of high CO flux (Figure 6, $x_{CO} \geq 0.5$), the TOF for the type II aggregates even exceeds the value for the large Pd crystallites. This behavior indicates a reduced CO-induced poisoning in the case of the small aggregates. We can tentatively relate this difference to the modified CO adsorption behavior of the small particles. In previous adsorption studies (XAS and high-resolution PES) it has been shown that on such aggregates the strength of the CO−Pd bond exhibits a more pronounced coverage dependence.[25,44,48] Therefore, we may expect that on the large and ordered islands of type I the CO coverage builds up rapidly once the CO-rich regime is reached. On more disordered particles a broader range of adsorption energies exist. Therefore, these lower binding energy sites will be more slowly occupied with increasing CO flux and some of them may not be occupied even for the largest x_{CO} values, yet still be relevant with respect to oxygen adsorption. Thus, we may expect that the surface of the smaller Pd particles (type II) will be less easily poisoned under CO-rich conditions.

Note that the modified transient behavior is qualitatively consistent with these suggestions: Besides the more strongly bound CO, a fraction of CO with a lower activation barrier toward desorption and/or reaction is assumed to coexist. A rapid depletion of this species will occur upon termination of the CO beam. This will give rise to the sudden decrease in the reaction rate over a wide range of flux conditions. The decrease will be followed by a CO_2 production peak of reduced intensity, which arises from the remaining (regular) CO species. Please note that the more weakly bound CO may represent a minority species but—depending on the reaction barrier, which may also be reduced with respect to the regular sites—may still dominate the reaction rate. Indeed, a time-resolved IRAS experiment equivalent to the one reported for the type I particles[42] shows no indication for a large decrease in the CO coverage directly after termination of the CO beam. More detailed experiments in combination with kinetic simulations taking into account the presence of different types of adsorption sites are currently in progress and will help to clarify these points.

3.3. In Situ IR Absorption Spectroscopy under Steady-State Conditions. To obtain additional insight into the occupation of adsorption sites on the different particles, we have performed in situ IRA spectroscopy under steady-state conditions. The spectra were recorded after the steady state was reached in a transient measurement of the type displayed in Figure 4. The spectra of the CO stretching frequency region

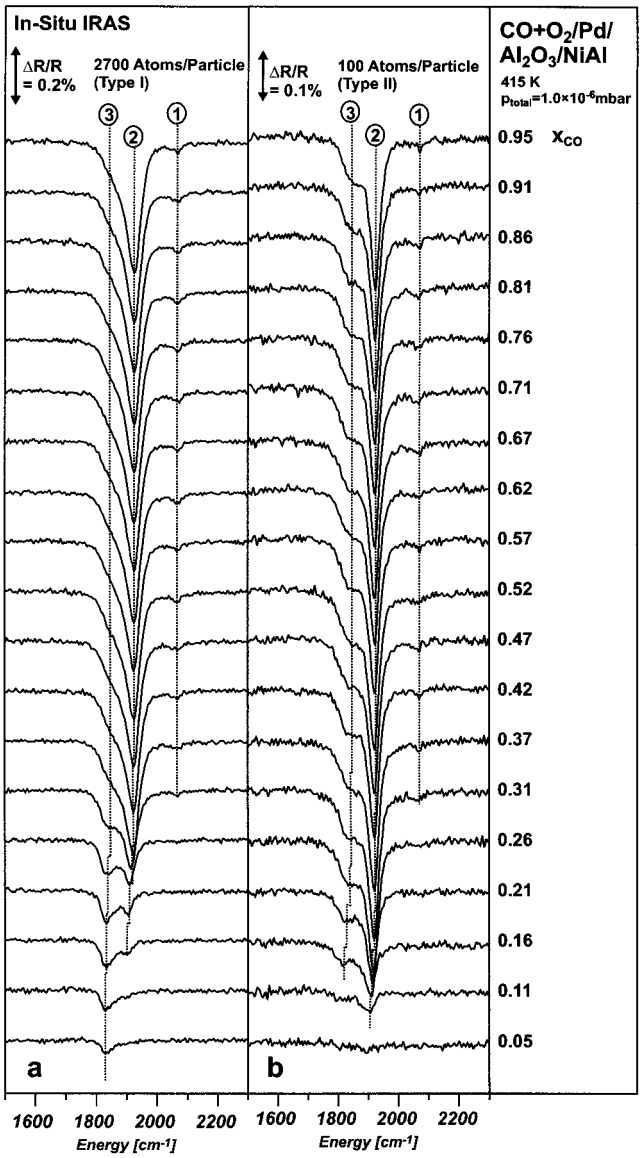

Figure 7. In situ IR reflection absorption spectra under steady-state reaction conditions as a function of the CO fraction in the impinging gas flux x_{CO} for two different average particle sizes: (a) 2700 atoms/particle (Table 1, type I); (b) 100 atoms/particles (Table 1, type II) ($T_{sample} = 415$ K, $p_{total} = 1.0 \times 10^{-6}$ mbar).

for particles of types I and II are compared in Figure 7 (reaction temperature of 415 K). Briefly, three types of CO can be distinguished for both experimental situations: (1) A weak feature at ~2060 cm^{-1} can be assigned to CO bonded to Pd on-top sites (Figure 7, no. 1), possibly of defect nature;[25,42] (2) a feature between 1900 and 1930 cm^{-1}, which is assumed to contain contributions from CO on 3-fold hollow sites on (111) facets[59] and bridge-bonded CO, in particular on defect sites and Pd(100) facets[26,60] (Figure 7, no. 2); and (3) features between 1815 and 1870 cm^{-1} originating from CO adsorbed on more highly coordinated hollow sites (Figure 7, no. 3). For a detailed discussion we refer to the literature (see refs 25, 26, 42, and 60 and refs therein). In this work we will again focus on particle size dependencies under reaction conditions, only.

Characteristic changes in the IR spectra as a function of the CO flux fraction x_{CO} are observed, which are illustrated in the insets in Figure 6. We compare two sets of spectra, the absorption under oxygen-rich ($x_{CO} = 0.21$) and CO-rich conditions ($x_{CO} = 0.91$). Whereas the relative intensity of the

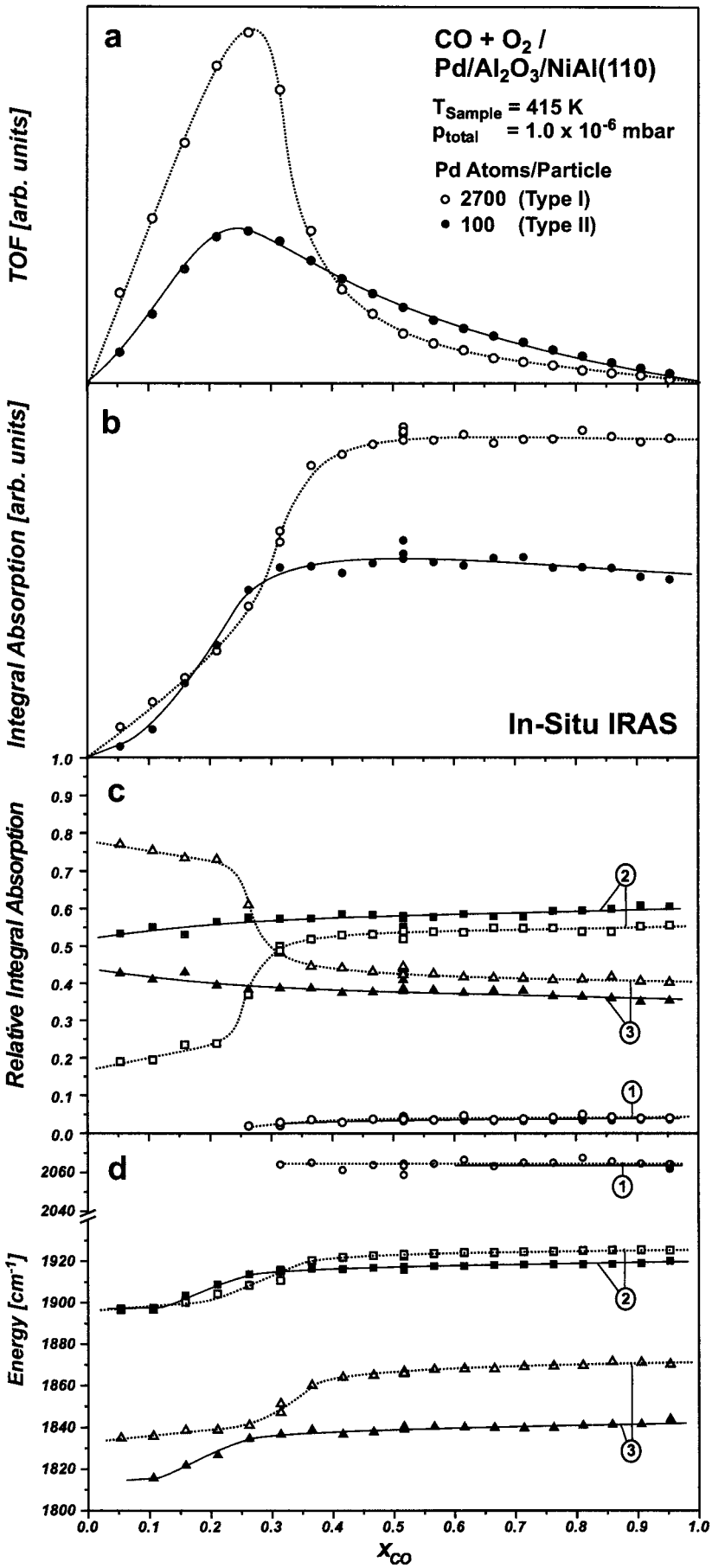

Figure 8. (a) Steady-state turnover frequencies (TOF), (b) the integrated absorption for the IR spectra presented in Figure 7, (c) the relative absorption of the characteristic absorption features marked in Figure 7, and (d) vibrational frequencies of the CO absorption features. Two different particle sizes are compared (open symbols, 2700 atoms/particle, Table 1, type I; solid symbols, 100 atoms/particle, Table 1, type II).

absorption features for the small particles (type II) appears similar under both conditions (the high-energy feature at ~1920 cm^{-1} always dominates the spectrum), drastic changes are observed for the larger particles of type I. Under conditions of low CO flux, the low-frequency absorption feature (~1840 cm^{-1}) dominates, but with increasing x_{CO}, the intensity ratio becomes similar to the spectra of CO on type II Pd particles.

In a more quantitative manner, the development of the absorption features is summarized in Figure 8. The development of the integral IR absorption as a function of x_{CO} is displayed in Figure 8b: Initially, the CO signal increases slowly with increasing CO flux fraction (oxygen-rich regime). In the transition region, where the systems switches to the CO-rich reaction regime, the CO absorption signal increases more rapidly, indicating a sudden rise in the CO coverage. From this point on, hardly any further changes can be detected. The coverage change is also reflected in the increasing stretching frequencies (Figure 8d), which may serve as a measure for the local CO density.[61] The lower absorption level for the type II particles is qualitatively consistent with the lower surface atom density in this case. It has to be pointed out, however, that a quantitative determination of the coverage from the IR absorption is not straightforward, since the absorption may become rather coverage-insensitive at high CO densities (see ref 61). These difficulties may be illustrated by considering the IR spectra and reaction rate in the CO rich regime (Figure 8): The reaction rate decreases nonlinearly, indicating an increasing CO poisoning effect, i.e., an increasing CO coverage. Still no increase in the total absorption is found for $x_{CO} > 0.45$ (for both types of Pd particles). This is a consequence of the fact that only a small fraction of the CO sites is additionally occupied and their differential IR absorption cross section is small (at high CO coverage). Due to these difficulties, we restrict the following discussion to the more fundamental and qualitative features.

As discussed before, drastic differences for the two particle types are found with respect to the relative intensity of the features (Figure 8c). For the small particles (type II) we observe a dominating feature in the frequency region between 1900 and 1930 cm^{-1} over the full range of flux conditions investigated. Only weak changes in the site occupation are detected upon changing from the oxygen-rich to the CO-rich regime. A entirely different behavior is found for the large particles of type I. Whereas under oxygen-rich reaction conditions absorption in the low-frequency region (1835−1870 cm^{-1}) dominates and the absorption signal at higher frequency is weak, the situation is reversed once the transition regime is reached. At the same time distinct differences are observed with respect to the CO stretching frequencies of the 3-fold hollow species (Figure 8d, no. 3), which appear to be shifted to lower frequencies by ~25 cm^{-1} for the smaller particles.

The differences as a function of CO flux may be rationalized, if we take into account the characteristics of CO adsorption on a Pd(111) single-crystal surface. Characteristic for this surface is that several adsorption sites will yield similar CO adsorption energies. As a consequence, a large number of adsorption structures may be formed as a function of coverage, giving rise to a variety of IR absorption bands. At low coverage CO adsorbs in fcc 3-fold hollow sites, changing to a mixture of fcc and hcp 3-fold hollow sites at higher coverage.[59] Proceeding to even higher coverage, the adsorption site changes to bridge and finally back to the hollow and additional on-top sites (see refs 46, 62, and 63 and refs therein). Although, differences with respect to the Pd(111) single crystal are observed, in particular at low temperatures and high adsorbate coverages,[60] the adsorbate layer on the large type I particles exhibits a similar flexibility with respect to rearrangements as a function of coverage.

In contrast to this, on the smaller defect-rich particles of type II, this type of adsorbate restructuring appears to be suppressed. Instead, the relative occupation of sites remains similar, although both the global and local adsorbate density increases with increasing CO flux (see integral absorption and frequency shift, Figure 8b and 8d). The difference may be tentatively related to the higher density of defect sites. Larger differences in the CO adsorption energy with a fraction of the CO adsorbed at preferred defect sites may lock the CO adsorbate layer and thus prevent global rearrangements in a similar fashion as observed on a single crystal.

Naturally, such a adsorbate layer will be not as homogeneous as on the single crystal. The remaining vacant adsorption sites may then facilitate oxygen adsorption under conditions where the reaction on the single crystal would be largely poisoned by the CO layer. Thus, in addition to the oxygen adsorption behavior discussed in the previous section, the modified CO adsorption could contribute to the reduced poisoning on small Pd particles under CO-rich conditions.

4. Conclusions

Using molecular beam techniques combined with in situ IRA spectroscopy we have studied the CO oxidation kinetics on Pd/alumina model catalysts.

We have compared two types of Pd particles with average particle sizes of 100 and 2700 Pd atoms/particle, respectively, which were grown under UHV conditions on a well-ordered alumina film on NiAl(110).

Using a combination of two beam sources crossed on the sample surface, we have studied the reaction rates as a function the of CO and oxygen fluxes and at surface temperatures between 415 and 465 K, performing both transient and steady-state measurements. The experiments indicate that the reactivity of the small particles is modified, both under oxygen-rich and CO-rich conditions.

We have performed in situ IR absorption spectroscopy under steady-state conditions in order to probe the occupation of different types of adsorption sites on the supported particles. For the large and well-ordered crystallites, pronounced rearrangements in the CO adsorbate layer are observed as a function of the applied CO and O_2 flux. No such site changes can be detected for the small aggregates.

On the basis of previous adsorption studies, it is suggested that the reduced activity under oxygen-rich conditions is related to an enhanced interaction of oxygen with the small aggregates. Under CO-rich conditions, a weaker poisoning effect is observed, which is suggested to be connected to the enhanced coverage dependence of the CO−Pd bond strength and the resulting lower flexibility of the CO adsorbate layer.

Acknowledgment. This project has been funded by the Max-Planck-Society and the Deutsche Forschungsgemeinschaft. We would like to thank Dr. M. Frank and Dr. M. Bäumer for the STM data used in this work. Moreover, we would like to thank Prof. Dr. C. R. Henry for many useful discussions. H.-J. F. is grateful for his support from CNRS as chercheur associé at CRMC2-CNRS in Luminy.

References and Notes

(1) Ertl, G.; Knoezinger, H.; Weitkamp, J. *Handbook of Heterogeneous Catalysis*; VCH: Weinheim, 1997.

(2) Che, M.; Bennett, C. O. *Adv. Catal.* **1989**, *20*, 153.
(3) Mason, M. G. *Phys. Rev. B* **1983**, *27*, 748.
(4) Wertheim, G. K. *Z. Phys. D* **1989**, *12*, 319.
(5) Henry, C. R.; Chapon, C.; Goyhenex, C.; Monot, R. *Surf. Sci.* **1992**, *272*, 283.
(6) Henry, C. R. *Surf. Sci. Rep.* **1998**, *31*, 231.
(7) Hayek, K.; Kramer, R.; Paál, Z. *Applied Catalysis A* **1997**, *162*, 1.
(8) Ogawa, S.; Ichikawa, S. *Phys. Rev. B* **1995**, *51*, 17231.
(9) Rupprechter, G.; Seeber, G.; Goller, H.; Hayek, K. *J. Catal.* **1999**, *186*, 201.
(10) Pacchioni, G.; Rösch, N. *Surf. Sci.* **1994**, *306*, 169.
(11) Pajonk, G. M. In *Handbook of Heterogeneous Catalysis*; Ertl, G., Knözinger, H., Weitkamp, J., Eds.; VCH: Weinheim, 1997; Vol. 3.
(12) Conner, W. C.; Falconer, J. L. *Chem. Rev.* **1995**, *95*, 759.
(13) Zhdanov, V. P.; Kasemo, B. *Surf. Sci. Rep.* **2000**, *39*, 25.
(14) Zhdanov, V. P.; Kasemo, B. *Surf. Sci.* **1998**, *405*, 27.
(15) Zhdanov, V. P.; Kasemo, B. *J. Catal.* **1997**, *170*, 377.
(16) Goodman, D. W. *Surf. Rev. Lett.* **1995**, *2*, 9.
(17) Freund, H.-J.; Bäumer, M.; Kuhlenbeck, H. *Adv. Catal.* **2000**, *45*, 333.
(18) Bäumer, M.; Libuda, J.; Sandell, A.; Freund, H.-J.; Graw, G.; Bertrams, T.; Neddermeyer, H. *Ber. Bunsen-Ges. Phys. Chem.* **1995**, *99*, 1381.
(19) Bäumer, M.; Libuda, J.; Freund, H.-J. In *Chemisorption and Reactivity on Supported Clusters and Thin Films*; Lambert, M., Pacchioni, G., Eds.; Kluwer Academic Press: 1997; p 61.
(20) Rainer, D. R.; Goodman, D. W. *J. Mol. Catal. A* **1998**, *131*, 259.
(21) Freund, H.-J. *Angew. Chem., Int. Ed. Engl.* **1997**, *36*, 452.
(22) Jaeger, R. M.; Kuhlenbeck, H.; Freund, H.-J.; Wuttig, M.; Hoffmann, W.; Franchy, R.; Ibach, H. *Surf. Sci.* **1991**, *259*, 235.
(23) Libuda, J.; Winkelmann, F.; Bäumer, M.; Freund, H.-J.; Bertrams, T.; Neddermeyer, H.; Müller, K. *Surf. Sci.* **1994**, *318*, 61.
(24) Jaeger, R. M.; Libuda, J.; Bäumer, M.; Homann, K.; Kulenbeck, H.; Freund, H.-J. *J. Electron Spectrosc. Relat. Phenom.* **1993**, *64*/*65*, 217.
(25) Bäumer, M.; Freund, H.-J. *Prog. Surf. Sci.* **1999**, *61*, 127.
(26) Wolter, K.; Seiferth, O.; Kuhlenbeck, H.; Bäumer, M.; Freund, H.-J. *Surf. Sci.* **1998**, *399*, 190.
(27) Hansen, K. H.; Worren, T.; Stempel, S.; Laegsgaard, E.; Bäumer, M.; Freund, H.-J.; Besenbacher, F.; Stensgaard, I. *Phys. Rev. Lett.* **1999**, *83*, 4120.
(28) Asscher, M.; Somorjai, G. A. In *Atomic and Molecular Beam Methods*; Scoles, G., Ed.; Oxford University Press: 1988; Vol. 2, p 489.
(29) D'Evelyn, M. P.; Madix, R. J. *Surf. Sci. Rep.* **1984**, *3*, 413.
(30) Rettner, C. T.; Auerbach, D. J.; Tully, J. C.; Kleyn, A. W. *J. Phys. Chem.* **1996**, *100*, 13021.
(31) Barker, J. A.; Auerbach, D. J. *Surf. Sci. Rep.* **1985**, *4*, 1.
(32) Engel, T.; Ertl, G. *J. Chem. Phys.* **1978**, *69*, 1267.
(33) Engel, T. *J. Chem. Phys.* **1978**, *69*, 373.
(34) Campbell, C. T.; Ertl, G.; Kuipers, H.; Segner, J. *J. Chem. Phys.* **1980**, *73*, 5863.
(35) Brown, L. S.; Sibener, S. J. *J. Chem. Phys.* **1989**, *90*, 2807.
(36) Brown, L. S.; Sibener, S. J. *J. Chem. Phys.* **1988**, *89*, 1163.
(37) Stará, I.; Nehasil, V.; Matolín, V. *Surf. Sci.* **1996**, *365*, 69.
(38) Stará, I.; Nehasil, V.; Matolín, V. *Surf. Sci.* **1995**, *331*−*333*, 173.
(39) Becker, C.; Henry, C. R. *Catal. Lett.* **1997**, *43*, 55.
(40) Becker, C.; Henry, C. R. *Surf. Sci.* **1996**, *352*, 457.
(41) Meusel, I.; Hoffmann, J.; Hartmann, J.; Heemeier, M.; Bäumer, M.; Libuda, J.; Freund, H.-J. *Catal. Lett.* **2001**, *71*, 5.
(42) Libuda, J.; Meusel, I.; Hoffmann, J.; Hartmann, J.; Piccolo, L.; Henry, C. R.; Freund, H.-J. *J. Chem. Phys.* **2001**, *114*, 4669.
(43) Libuda, J.; Meusel, I.; Hartmann, J.; Freund, H.-J. *Rev. Sci. Instrum.* **2000**, *71*, 4395.
(44) Libuda, J. Ph.D Thesis, 1996.
(45) Bäumer, M.; Frank, M.; Libuda, J.; Stempel, S.; Freund, H.-J. *Surf. Sci.* **1997**, *391*, 204.
(46) Guo, X.; Hoffman, A.; Yates, J. T., Jr. *J. Chem. Phys.* **1989**, *90*, 5787.
(47) Szanyi, J.; Kuhn, W. K.; Goodman, D. W. *J. Vac. Sci. Technol. A* **1993**, *11*, 1969.
(48) Sandell, A.; Libuda, J.; Brühwiler, P. A.; Andersson, S.; Bäumer, M.; Maxwell, A. J.; Mårtensson, N.; Freund, H.-J. *Phys. Rev. B* **1997**, *55*, 7233.
(49) Graoui, H.; Giorgio, S.; Henry, C. R. *Surf. Sci.* **1998**, *417*, 350.
(50) Matolín, V.; Gillet, E.; Kruse, N. *Surf. Sci.* **1987**, *186*, L541.
(51) Piccolo, L.; Becker, C.; Henry, C. R. *Appl. Surf. Sci.* **2000**, 156.
(52) Engel, T.; Ertl, G. In *The Chemical Physics of Solid Surfaces and Heterogeneous Catalysis*; King, D. A., Woodruff, D. P., Eds.; Elsevier: 1982; Vol. 4, p 73.
(53) Weissman, D. L.; Shek, M. L.; Spicer, W. E. *Surf. Sci.* **1980**, *92*, L59.
(54) Weissman-Wenicur, D. L.; Shek, M. L.; Stefan, P. M.; Lindau, I.; Spicer, W. E. *Surf. Sci.* **1983**, *127*, 513.
(55) Surnev, L.; Bliznakov, G.; Kiskinova, M. *Surf. Sci.* **1984**, *140*, 249.
(56) Ladas, S.; Imbihl, R.; Ertl, G. *Surf. Sci.* **1989**, *219*, 88.
(57) Basset, M. R.; Imbihl, R. *J. Chem. Phys.* **1990**, *93*, 811.
(58) Ehsasi, M.; Seidel, C.; Ruppender, H.; Drachsel, W.; Block, J. H.; Christmann, K. *Surf. Sci.* **1989**, *210*, L198.
(59) Gieβel, T.; Schaff, O.; Hirschmugl, C. J.; Fernandez, V.; Schindler, K.-M.; Theobald, A.; Bao, S.; Lindsay, R.; Berndt, W.; Bradshaw, A. M.; Baddeley, C.; Lee, A. F.; Lambert, R. M.; Woodruff, D. P. *Surf. Sci.* **1998**, *406*, 90.
(60) Frank, M.; Bäumer, M. *Phys. Chem. Chem. Phys.* **2000**, *2*, 4265.
(61) Hoffmann, F. M. *Surf. Sci. Rep.* **1983**, *3*, 107.
(62) Tüshaus, M.; Berndt, W.; Conrad, H.; Bradshaw, A. M.; Persson, B. *Appl. Phys. A* **1990**, *51*, 91.
(63) Tüshaus, M. Ph.D Thesis, 1990.
(64) Frank, M.; Bäumer, M., unpublished.